Modeling Seismic Recordings of High-Frequency Guided Infrasound on Mars

Zongbo Xu, Marouchka Froment, Raphaël Garcia, Éric Beucler, Keisuke Onodera, Taichi Kawamura, Philippe Lognonné, William Bruce Banerdt

Modelling seismic recordings of high-frequency guided infrasound on Mars

Zongbo Xu[1], Marouchka Froment[1,2], Raphaël F. Garcia[3], Éric Beucler[4,5], Keisuke Onodera[6], Taichi Kawamura[1], Philippe Lognonné[1], William Bruce Banerdt[7]

[1] Université Paris Cité, Institut de physique du globe de Paris, CNRS, F-75005 Paris, France
[2]Earth and Environmental Sciences Division, Los Alamos National Laboratory, Los Alamos, NM 87545, USA
[3]Institut Supérieur de l'Aéronautique et de l'Espace (ISAE-SUPAERO), Université de Toulouse, 10 Ave E. Belin 31400 Toulouse, France
[4]Nantes Université, Université Angers, Le Mans Université, CNRS, UMR 6112, Laboratoire de Planétologie et Géosciences, F-44000 Nantes, France
[5]Nantes Université, UGE, Univ Angers, CNAM, CNRS, UAR 3281, Observatoire des sciences de l'univers Nantes Atlantique, F-44000 Nantes, France
[6]Earthquake Research Institute, The University of Tokyo 1-1-1 Yayoi, Bunkyo-ku, Tokyo, Japan
[7]Jet Propulsion Laboratory, California Institute of Technology, Pasadena, CA 91109, USA

Key Points:

- We analytically compute the dispersion relationship of guided infrasound in 1D atmospheric models from Mars and Earth;
- We model the ground response to guided infrasound to fit the corresponding seismic observation due to meteorite impacts on Mars;
- We utilize the seismic recording due to guided infrasound to constrain the subsurface structures.

Corresponding author: Zongbo Xu, zongboxu@ipgp.fr

Abstract

NASA's InSight mission records several high-frequency (>0.5 Hz) dispersive seismic signals on Mars. These signals are due to the acoustic-to-seismic coupling of infrasound generated by the entry and impact of meteorites. This dispersion property is due to infrasound propagating in a structured atmosphere, and we refer to this dispersive infrasound as guided infrasound. We propose to model the propagation of guided infrasound and the seismic coupling to the ground analytically; we use a 1D layered atmosphere on a three-layer solid subsurface medium. The synthetic ground movements fit the observed dispersive seismic signals well and the fitting indicates the regolith beneath InSight is about 40-m in thickness. We also examine and validate the previously-published subsurface models derived from InSight ambient seismic vibration data.

Plain Language Summary

Under particular weather conditions, the Martian atmosphere displays a special sound-wave velocity profile, where the wave velocity becomes larger with increasing altitude within a few hundred meters. When an infrasound signal - a low-frequency (<20 Hz) sound wave inaudible to humans - propagates through such a structure, the infrasound exhibits dispersion : its propagation velocity depends on its frequency. We refer to such infrasound as guided infrasound. Guided infrasound can deform the ground, and have been recorded by the seismometer of NASA's InSight mission on the Martian surface. We propose to model these recordings using the physics of sound waves traveling above a compliant solid ground. We show that our modelling results can fit well the seismic recordings of guided infrasound on Mars. We apply our modelling to the subsurface models from a different InSight seismic observation to check if these models can explain our seismic recordings. This modelling constitutes a new tool to investigate the subsurface structure of Mars, and is also useful for the investigation of Titan and Venus.

1 Introduction

NASA's InSight (Interior Exploration using Seismic Investigations, Geodesy and Heat Transport) mission landed on the Martian surface in November 2018 and has since been conducting geophysical and meteorological observation (Banerdt et al., 2020). To achieve its objectives, InSight is equipped with a Very Broad Band (VBB) and a Short Period (SP) seismometer, which together constitute the SEIS (Seismic Experiment for Internal Structure) instrument (Lognonné et al., 2019). SEIS is operated in combination with a weather station, Auxiliary Payload Sensor Suite (APSS) including an atmospheric pressure sensor and wind and temperature sensors, to perform meteorological observation (Banfield et al., 2019). Due to power issues appearing in the second Martian year of the mission, SP and APSS have become temporarily unavailable, and VBB has been kept on most of the time. Thus only the VBB seismic data is available for analyzing the seismic events in this study.

The ground motion recorded by InSight originates from different types of sources, most of which are marsquakes (e.g. Giardini et al., 2020) or atmospheric seismic events like pressure drops (e.g. Lognonné et al., 2020). The recent seismic recordings provides a new type of seismic events, a dispersive wave train following a typical very-high-frequency (VF) marsquake (Clinton et al., 2021), where a dispersive wave train means that the wave velocity, also arrival time, depends on frequency. This wave train appears about a few hundred of seconds after the P arrivals, such as in events S0793a, S0981c, and S0986c. Based on analysis of seismic arrival times and satellite imagery, Garcia et al. (2022) demonstrate that these events are generated by meteorite impacts on the Martian surface (Figure 1). Thus, the high-frequency seismic energy arriving before the dispersive waves is due to the meteorite cratering process (Figure 2a).

The meteors not only generate the craters but also interact with the Martian atmosphere during entry and impacting, which generates infrasound, i.e. acoustic waves with a frequency lower than 20 Hz (Figure 2). The infrasound propagation medium - the atmosphere - can exhibit a particular structure, where the infrasound propagation velocity is smaller near the ground surface than at higher altitudes (about a few hundred meters). In such structures, multiple infrasound propagation paths interfere with each other, and the interference generates dispersion (Herrin et al., 2006; Negraru & Herrin, 2009), similar to the mechanism of Love waves in seismology (e.g. Aki & Richards, 2002). This infrasound velocity model in Earth is referred to as nocturnal boundary layer in acoustic-wave literature (e.g. Waxler, 2004), since such a model is usually generated when the temperature on the ground surface decreases at night, leading to a cooling of the lower atmosphere. This phenomenon is common on Mars due to the quick cooling down of the Martian surface at night and/or high-altitude winds (e.g. Garcia et al., 2017). In this study, we refer to this atmospheric structure as a waveguide, and we refer to the interfered infrasound waves as guided infrasound. Guided infrasound can be simulated numerically by solving the acoustic wave equations (e.g. Garcia et al., 2017; Martire et al., 2020). This numerical simulation approach can address complicated atmospheric models like a laterally heterogeneous atmosphere with winds, but is computationally expensive. One can also model the guided infrasound waveform analytically by calculating the phase/group velocity (i.e. dispersion) within a laterally-homogeneous two-layer atmospheric model (Negraru & Herrin, 2009). This analytical approach is much faster and less computationally expensive than the numerical simulation, and is therefore well suited to explore different atmospheric parameters and their associated guided infrasound. However, former studies remain limited to two-layer atmospheric models. In this study, we extend this analytical approach to a multiple-layer model using the propagation matrix method described in seismic surface-wave studies (e.g. Aki & Richards, 2002). Note that in this study we focus on the high-frequency guided infrasound, while on Earth, the low-frequency (<0.02 Hz) guided infrasound also exists (e.g. Pekeris, 1948; Press & Harkrider, 1962; Harkrider, 1964).

We use the VBB seismic data (InSight Mars SEIS Data Service, 2019a, 2019b) to study guided infrasound observed on Mars, because infrasound propagates with atmospheric perturbations and the perturbations deform the ground (e.g. Sorrells, 1971; Tanimoto & Wang, 2019). One has observed this type of coupling due to atmospheric pressure drops through seismic recordings on both Earth and Mars (e.g. Lorenz et al., 2015; Lognonné et al., 2020; Kenda et al., 2020). Furthermore one also observes infrasound deforming Earth's ground surface due to acoustic sources such as volcanic activities (e.g. Ichihara et al., 2012), meteors (e.g. Edwards et al., 2008), and ground surface explosions (e.g. Gibbons et al., 2007; Schneider et al., 2018). Conversion of an atmospheric pressure perturbation into ground deformation is called compliance, and the intensity of compliance is determined by the subsurface structure and the propagation velocity of the perturbation (e.g. Ewing et al., 1957; Sorrells et al., 1971; Ben-Menahem & Singh, 2012). We detail computation of compliance in Section 3.

We propose to analytically model the seismic recordings due to guided infrasound, and we refer to the recordings as chirps. We demonstrate computation of the guided infrasound phase and group velocities in multiple-layer atmospheric models (Section 2). We then introduce the compliance and our subsurface velocity model (Section 3). We combine the guided infrasound and the compliance to generate a synthetic chirp; we use the synthetic chirp to fit the observed ones (Section 4). We finally discuss the implication of our modelling to the previously-published subsurface models and the infrasound propagation in the Martian atmosphere (Section 5). Our research can aid the investigation of atmospheric and subsurface properties, not only on Mars and Earth but also on other bodies with atmosphere such as Titan and Venus.

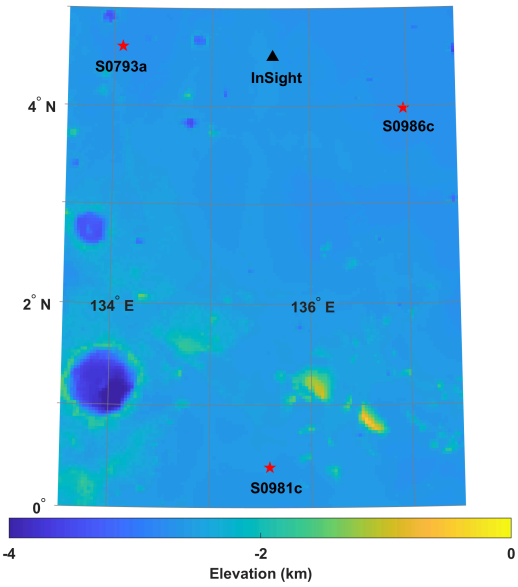

Figure 1. Topography map (Smith et al., 2001) of the Martian surface around InSight and three impact locations (S0793a, S0981c, and S0986c). The impact locations are constrained by CTX images (Garcia et al., 2022).

2 Modelling Guided infrasound

2.1 Theory

We solve the dispersion of the guided infrasound in a multiple-layer atmospheric model theoretically. We present an example of the Martian guided infrasound in this section and an Earth example in Appendix A. We assume the atmosphere to be adiabatic, which leads to the following 2D governing equations:

$$-\partial_z p = \rho D_t v_z, \tag{1}$$

$$-\partial_x p = \rho D_t v_x, \tag{2}$$

$$-D_t p = K(\partial_z v_z + \partial_x v_x), \tag{3}$$

where ∂_z denotes the partial derivative with respect to altitude (z), p is the atmospheric pressure perturbation conveyed by the infrasound wave, ρ is the air density, and K is the incompressibility; v_z and v_x are the particle velocities in the vertical and horizontal directions, respectively. D_t denotes the material derivative with respect to time. Indeed, the advection of momentum cannot be ignored here, as the horizontal wind velocity (w_x) can reach up to about 15 m/s on the Martian surface. The effect of w_x is made explicit by rewriting the above equations as:

$$-\partial_z p = \rho(\partial_t + w_x\partial_x)v_z, \tag{4}$$

$$-\partial_x p = \rho(\partial_t + w_x\partial_x)v_x, \tag{5}$$

$$-(\partial_t + w_x\partial_x)p = K(\partial_z v_z + \partial_x v_x). \tag{6}$$

Since in the three impact events, the cross winds deviate the infrasound propagation direction by less than 5 deg (Garcia et al., 2022), we neglect the cross wind effect and project the total wind speed to the guided infrasound propagation direction to achieve w_x (Table S1, S2, and S3). Besides the above equations, a set of boundary conditions is also needed. We adopt a rigid ground surface, such as:

$$v_z(z = 0) = 0. \tag{7}$$

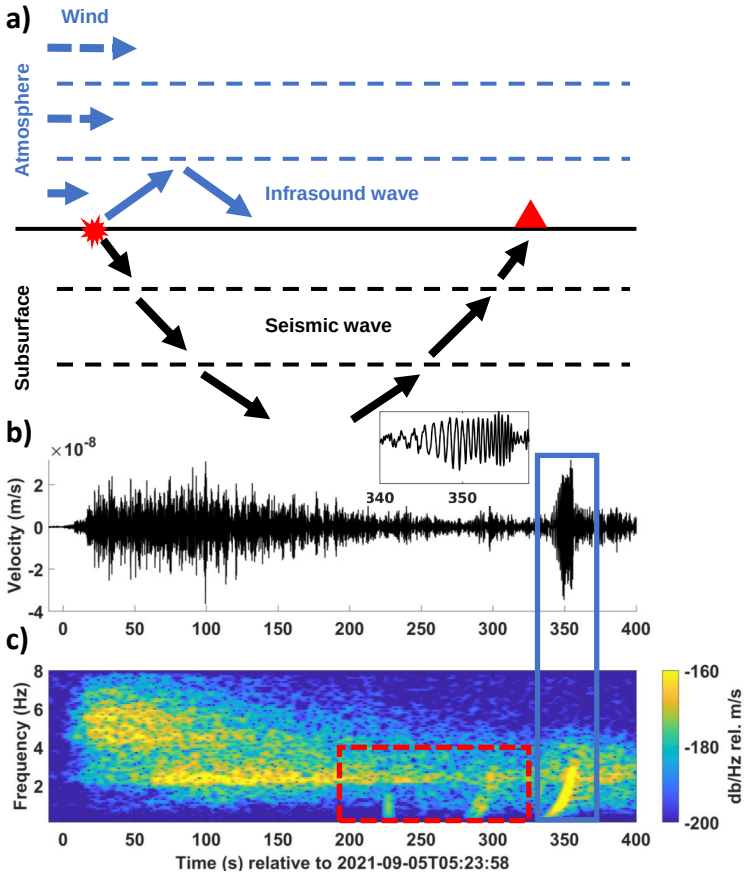

Figure 2. Illustration of the S0986c event (a) and data (b, c). (a) The meteor of the S0986c impact interacts with the Martian subsurface and atmosphere, generating seismic waves (from 0 to about 200 s in (b) and infrasound (after 200 s in b), respectively. The vertical scales of the atmosphere and the subsurface are in hundred meter and kilometer, respectively. (b) The S0986c VBB vertical-component data. The data is bandpass filtered between 0.1 and 8 Hz. The insert shows a zoom of the chirp in the blue box. (c) Spectrogram of the data in (b). The blue box indicates the chirp spectrogram. The red box indicates other arrivals of infrasound energy. The time axis is in Coordinated Universal Time (UTC).

Note that one may choose an elastic ground-surface boundary condition and then the right hand side of the above equation would not be zero anymore (e.g. Waxler, 2002). We justify our rigid boundary condition in Section 5.3. We use the radiation boundary condition for the top boundary. The 2D geometry assumed here is a good approximation for a real 3D geometry only if the cross-wind can be neglected (e.g. Nijs & Wapenaar, 1992). Other second-order factors are not considered here, such as the effect of static pressure or gravity (e.g. Pierce, 1990).

We compute the guided infrasound phase velocities by solving the above equations (Equation 4, 5 and 6) and the boundary conditions (e.g. Equation 7). One can adopt normal mode expansion to solve the equations, and Assink (2012) present a complete review of this approach mathematically. However, this approach is not designed specifically for guided infrasound and is built on an elastic boundary condition, instead of our rigid one (Equation 7). Thus, we propose a simpler method. We assume that guided infrasound propagates horizontally as a plane wave:

$$p = P(\omega, z)\exp(i(\omega t - kx)), \tag{8}$$
$$v_z = V_z(\omega, z)\exp(i(\omega t - kx)), \tag{9}$$
$$v_x = V_x(\omega, z)\exp(i(\omega t - kx)), \tag{10}$$

where ω is the angular frequency, z is altitude, t is the propagation time, k is the horizontal wavenumber, and x is the propagation distance. Note that ω/k gives the phase velocity. Based on Equation 5, 8, and 10, we notice that

$$V_x = \frac{kP}{\rho(\omega - w_x k)}. \tag{11}$$

We then rewrite the governing equations in a matrix form as

$$\partial_z \begin{bmatrix} P \\ V_z \end{bmatrix} = \begin{bmatrix} 0 & -i(\omega - w_x k)\rho \\ -i\omega/\alpha^2/\rho + iw_x k/\rho/\alpha^2 + ik^2/(\omega - w_x k)/\rho & 0 \end{bmatrix} \begin{bmatrix} P \\ V_z \end{bmatrix}, \tag{12}$$

where α is the infrasound velocity, where $\alpha^2 = K/\rho$. Note that Press and Harkrider (1962) and Nijs and Wapenaar (1990) have achieved similar equations as Equation 12. Press and Harkrider (1962) study the low-frequency (<0.02 Hz) guided infrasound considering gravity, and Nijs and Wapenaar (1990) study acoustic wave propagation and do not consider the guided infrasound.

We use the propagation matrix method (e.g. Aki & Richards, 2002) to solve Equation 12. This equation is in the form of $\partial_z \vec{f} = \mathbf{A}\vec{f}$, where $\vec{f}$ is normally referred to as eigenfunctions and $\vec{f}$ here contains P and V_z. The propagation matrix is defined as $\mathbf{M}(z, z') = \exp\left[(z - z')\mathbf{A}\right]$ between two depths, z and z'. We use $\mathbf{M}$ to calculate the eigenfunctions at z from z' as

$$\vec{f}(z) = \mathbf{M}(z, z')\vec{f}(z'). \tag{13}$$

We observe that Equation 13 intuitively satisfies Equation 12. For a 1D atmospheric model, with a right phase velocity (i.e. ω/k) at frequency ω, we can calculate the eigenfunctions at all altitudes, and the eigenfunction values on the ground surface would satisfy the boundary condition (Equation 7). The computation is detailed in Section S1. Based on the phase velocity, we can also compute the group velocity as the variation of ω over the variation of k (e.g. Aki & Richards, 2002).

2.2 S0986c guided infrasound

We use an atmospheric model of Mars to illustrate the eigenfunctions and the group velocities of the S0986c guided infrasound (Figure 3). We adopt the atmospheric model parameters (acoustic-wave velocity, wind speed, air density, and altitude) from the Mars

Climate Database (MCD, Millour et al., 2018). We project the wind speed along the back-azimuth of SEIS with regards to the S0986c impact location (Figure 1 and Table S3); the cross wind of this event atmospheric model does not obviously affect the infrasound propagating from the impact location to InSight (Garcia et al., 2022). Note that MCD models the Martian climate at a global scale and could be biased at local scale like our cases. Thus we modify the acoustic-wave velocity by fitting the synthetic group velocity to the measurement from the chirp (Garcia et al., 2022). We add (subtract) a constant value to (from) acoustic-wave velocities at all altitudes, which moves the whole synthetic group-velocity curve up (down) but does not change the synthetic group-velocity shape (Figure 3c). The sum of the projected wind speed and the modified acoustic-wave velocity is called the effective velocity (Figure 3a). The effective velocity of this event increases gradually with altitude until about 500 m and then decreases slightly. We discretize the wind speed and the acoustic-wave velocity to form a 1D layered model, and then compute the phase velocity (Figure 3c) and the atmospheric pressure eigenfunctions (P, Figure 3b). The pressure eigenfunctions are real valued and maximal on the ground surface. We also observe that a high-frequency (3 Hz) eigenfunction decays faster than a low frequency one (1 Hz) with increasing altitude. The pressure eigenfunction represents the amplitudes (P in Equation 8) of the guided infrasound at different altitudes. For example, in this case, we would receive a lower-amplitude guided infrasound with an atmospheric-pressure sensor at 500 m altitude (like a balloon) compared to a sensor on the ground surface. The eigenfunctions also represent the excitation amplitude of the guided infrasound due to the source-receiver reciprocity (e.g. Landau & Lifshitz, 2013; Aki & Richards, 2002). Therefore an infrasound source at 500 m would generate weaker infrasound compared to a source on the ground surface. We use the phase velocity later in our computation of compliance (Section 3) and our chirp modelling (Section 4).

2.3 Higher-mode guided infrasound

We present the fundamental-mode guided infrasound in the above. The fundamental-mode represents the lowest-phase-velocity root in solving Equation 12 at each frequency, while the higher-velocity roots may also exist (Figure S1) and are referred to as the higher modes. The fundamental mode usually dominates guided infrasound in observations (e.g. Negraru & Herrin, 2009). Thus in the group-velocity measurement of S0981c and S0986c, we only observe the trends corresponding to the fundamental modes (Figure S1b and S1c).

We also demonstrate the domination of the fundamental-mode by computing the contribution of both the fundamental and higher modes to the pressure on the ground surface as $P^2(z=0)/\int P^2(z)dz$. The pressure eigenfuntion (P) is real valued if the corresponding mode is a trapped mode (e.g. Lognonné et al., 1998; Chakravarthy, 2008). However, at some frequencies, the eigenfunctions become complex valued, and the imaginary parts represent the energy leakage of the guided infrasound to the top halfspace (e.g. Press & Harkrider, 1962; Radovich & De Bremaecker, 1974). Thus we only use the real part of the eigenfunctions on the ground surface in computing the contributions (Figure S1). We observe that for S0981c and S0986c, the contribution of the fundamental modes are at least one magnitude (a factor of ten) larger than the higher modes at each frequency. However, for S0793a, the 1st-higher mode contributes more than the fundamental mode. We investigate this phenomenon in detail in Section 5.2.

3 Compliance: acoustic-to-seismic conversion

Atmospheric pressure perturbations, e.g. caused by wind or infrasound, can deform the ground at shallow depths on planets with atmosphere (e.g. Sorrells, 1971; Ben-Menahem & Singh, 2012), like the atmospheric noise recorded by SEIS on Mars (Lognonné et al., 2020; Garcia et al., 2020; Stutzmann et al., 2021). Furthermore, when the infrasound hor-

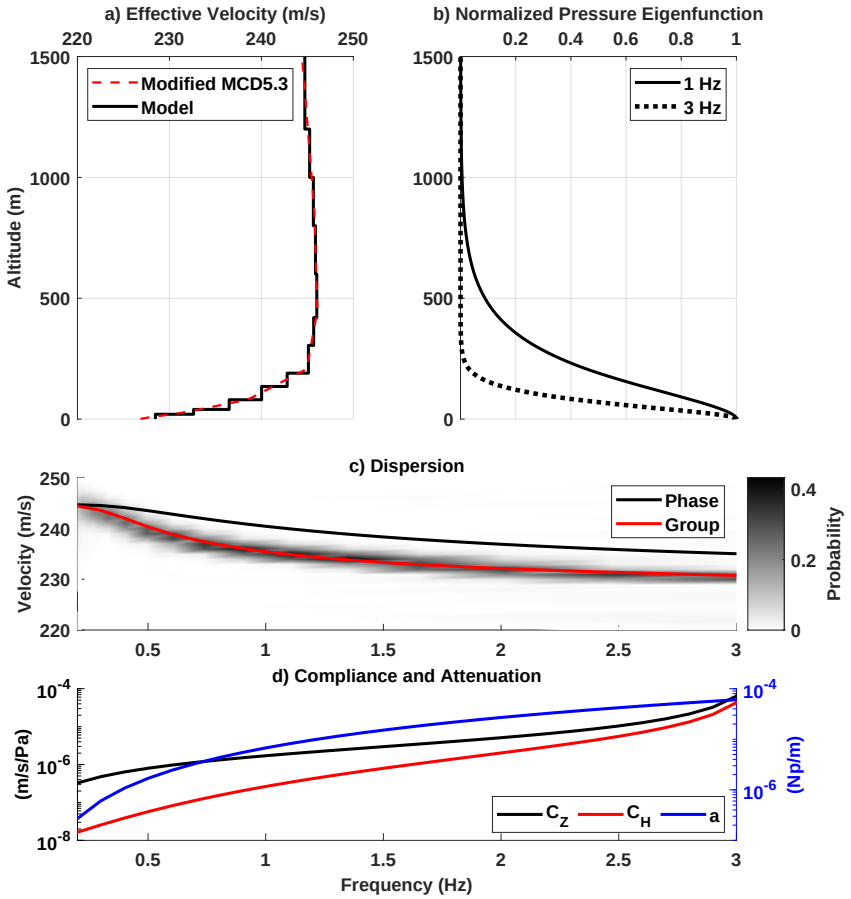

Figure 3. The infrasound velocity model (a), eigenfunctions (b), dispersion (c) and compliance (d) for S0986c. (a) We compute the infrasound velocity and the wind speeds from MCD for S0986c (Millour et al., 2018) and subtract 4 m/s from the velocity at all altitudes (red dashed line). The black line represents our 1D layered model. (b) Two different-frequency pressure eigenfunctions are normalized by each maximum value for visualization. (c) The gray background is the group-velocity measurement of the S0986c chirp (Garcia et al., 2022). (d) The vertical (black) and horizontal (blue) compliance is based on the phase velocity (c) and a subsurface velocity model (Table 1). The infrasound attenuation (blue) is from Bass and Chambers (2001) for 200 K temperature.

izontal apparent velocity is equal to the seismic-wave velocities of the subsurface, the infrasound would convert into seismic waves (e.g. Ewing et al., 1957; Langston, 2004). To summarize these different types of acoustic-to-seismic coupling, Edwards et al. (2008) list the possible conversion scenarios for homogeneous and isotropic elastic subsurface media. Note that in this study, we mainly focus on the so-called normal coupling, i.e. atmospheric pressure perturbations deforming the ground surface without generating seismic waves, but the following theory remains applicable to all the scenarios mentioned above. Due to the frequency band we use (here from 0.5 to about 2 Hz), we only consider the compliance in this study and ignore other effects like tilt (Garcia et al., 2020).

Compliance is the amplitude relationship between the pressure perturbation and the ground deformation. Compliance is determined by the subsurface structure and the propagation velocity of the pressure perturbation in the atmosphere overlaying the subsurface (e.g. Sorrells, 1971; Ewing et al., 1957; Ben-Menahem & Singh, 2012), based on the assumption that the perturbation propagates like a plane wave. Note that the plane-wave assumption even holds for a complex pressure wavefield, since the complex wavefield can be decomposed into plane waves (e.g. Kenda et al., 2017). In the subsurface media, the ground motion and normal stress (τ_{zz}) are defined as:

$$u_z(z) = U_z(\omega, z)\exp(i(\omega t - kx)), \tag{14}$$

$$u_x(z) = iU_x(\omega, z)\exp(i(\omega t - kx)), \tag{15}$$

$$\tau_{zz}(z) = T_{zz}(\omega, z)\exp(i(\omega t - kx)), \tag{16}$$

where u_z and u_x are the vertical and horizontal ground velocities, respectively; ω, k, t, and x are the same as in guided infrasound (Equation 8) while z here is the depth below the surface. The i in front of U_x in Equation 15 represents the $\pi/2$ phase shift between the horizontal and vertical components of the ground motion (e.g. Sorrells, 1971). We then write compliance as the amplitude ratio of the vertical (horizontal) ground velocities over the atmospheric pressure perturbation:

$$C_z = \frac{u_z(z=0)}{p(z=0)} = \frac{U_z(\omega, z=0)}{P(\omega, z=0)} = -\frac{U_z(\omega, z=0)}{T_{zz}(\omega, z=0)},, \tag{17}$$

$$C_x = \frac{u_x(z=0)}{p(z=0)} = \frac{iU_x(\omega, z=0)}{P(\omega, z=0)} = -\frac{iU_x(\omega, z=0)}{T_{zz}(\omega, z=0)}, \tag{18}$$

where $T_{zz}(z=0) = -P(z=0)$ (Equations 8 and 16) implies the continuity of normal stress on the ground surface. The minus sign is due to the different sign conventions between atmospheric studies and seismology. In acoustics wave studies (Section 2), the atmospheric pressure compressing the ground surface is defined as being positive, i.e. exerting a force in the vertically downward direction on the ground surface. However in seismology, a positive normal stress acting on a surface corresponds to a traction in the outward normal direction, i.e. the vertically upward direction on the flat ground surface. Note that here we refer to the vertical ground velocity as u_z, not to be mistaken with the vertical particle velocity in the atmosphere, i.e. v_z in Section 2.

To calculate the compliance values, we use the equation of motion and Hooke's law in 1D media (e.g. Aki & Richards, 2002, Chapter 7.2) and the zero-shear-stress boundary condition on the ground surface:

$$\tau_{zx} = 0. \tag{19}$$

Our computation is similar to Tanimoto and Wang (2019) where one does not assume the propagation velocity of pressure perturbation much slower than the shear-wave velocity of the subsurface medium. In this study, we use a three-layer velocity model simplified from the shallow (<100 m) geological structure under InSight (e.g. Warner et al., 2022). The first layer is made of thin soft regolith, as suggested by the analyses of the Martian atmospheric pressure drops (Kenda et al., 2020; Onodera, 2022) and of the hammerings of InSight's Heat Flow and Physical Properties (HP^3) instrument (Lognonné

Table 1. Parameters for a three-layer subsurface. The first two layers are regolith. In the first two layers, we calculate V_P from V_S based on the 0.22 Poisson's ratio (e.g. Morgan et al., 2018) ; we compute the density applying Gardner's empirical relationship (Gardner et al., 1974) to V_P.

Layer number	$V_P(m/s)$	$V_S(m/s)$	Density (kg/m^3)	Thickness (m)
1	117	70	1019	0.6
2	384	230	1372	40
3	3000	1700	2760	∞

et al., 2020). This surface layer is interpreted as fine-sand-dominated regolith. The second layer possesses a higher wave velocity than the first layer and represents coarse regolith (e.g. Warner et al., 2017). The third layer (i.e. halfspace) corresponds to the bedrock, composed of fractured basalt (e.g. Morgan et al., 2018). We use this three-layer model to compute compliance in the waveform modelling (Section 4). We achieve the parameters of the second layer through a waveform fitting in Section 4. Note that this model is simple and may not reflect the complexity of the real subsurface under InSight. We discuss possible improvement to this model in Section 5.4.

We notice that the difference of vertical velocities on the ground surface between the atmosphere and the subsurface give rise to a contradiction. In Section 2, we assume the vertical atmosphere velocity on the ground surface to be zero (Equation 7). The particle velocity should be continuous at the fluid-solid (i.e. atmosphere-ground) interface, and thus $u_z(z=0)=0$. However, a nontrivial compliance requires the vertical movements of the ground surface to be non-zero, i.e. $u_z(z=0)\neq 0$. We address this contradiction in Section 5.3. Note that such contradiction does not exist for the horizontal velocities, since the horizontal velocity of the ground surface is not necessarily continuous with the horizontal atmospheric particle velocity.

4 Waveform Forward modelling

We model synthetic chirp, the seismic recording due to guided infrasound, by combining the theories of guided infrasound (Section 2) and compliance (Section 3). The far-field synthetic ground velocity recordings of chirps (u) in the time domain are written as:

$$u_z = \mathscr{F}^{-1}\left[S(\omega)\exp\left(-ikx-ax\right)\frac{\exp\left(-i\pi/4\right)}{\sqrt{kx\pi/2}}\frac{P^2(\omega,0)}{\int P^2(\omega,z)dz}C_z(\omega)\right], \tag{20}$$

$$u_x = \mathscr{F}^{-1}\left[S(\omega)\exp\left(-ikx-ax\right)\frac{\exp\left(-i\pi/4\right)}{\sqrt{kx\pi/2}}\frac{P^2(\omega,0)}{\int P^2(\omega,z)dz}C_x(\omega)\right], \tag{21}$$

where $\mathscr{F}^{-1}$ denotes the inverse Fourier transform, and S is the source time function of guided infrasound. k is guided infrasound horizontal wavenumber and is from our calculation of the guided infrasound phase velocity (Section 2). x is infrasound travelling distance from the infrasound source to InSight (Table 2). a is the intrinsic attenuation coefficient for infrasound (Figure 2d and Bass & Chambers, 2001). $\exp\left(-i\pi/4\right)/\sqrt{kx\pi/2}$ is from the far-field approximation of a 3D cylindrical wave (e.g. Landau & Lifshitz, 2013). $P^2(\omega,0)/\int P^2(\omega,z)dz$ is the normalized pressure eigenfunction, representing the source excitation and sensor receiving on the ground surface. C_z (C_x) is the vertical (horizontal) compliance (Section 3). We use the three-layer subsurface velocity model (Table 1) in computing the compliance, where the model is from simplification of the shallow geological structure under InSight (e.g. Warner et al., 2022). We benchmark our modelling

Table 2. The origin time estimates and the geometry information of the three impact events relative to InSight (Garcia et al., 2022).

Event	Estimated origin time (UTC)	Distance (km)	Backazimuth (deg)
S0793a	2021-2-18T19:36:06	91.1	274.2
S0981c	2021-8-31T04:3:13	243.6	179.2
S0986c	2021-9-5T05:23:44	85.1	111.6

approach against a numerical simulation software, SPECFEM2D-DG (Martire et al., 2020), in Appendix B.

We use the synthetic chirp to fit the one due to an impact. We assume that the infrasound source generated by the meteor impacting is impulsive and thus the source time function (S in Equation 20 and 21) is a delta function in the time domain and a constant in the frequency domain. The source location is at the same location as the impact crater. Note that the source time function generated by a meteorite interacting with the Martian atmosphere in the impact is worth further investigation, but is beyond the scope of this study. Since the infrasound source is on the ground surface, we mainly observe the guided infrasound on InSight (Garcia et al., 2022).

We use the observed chirps from two events (S0981c and S0986c) in the fitting. For each event, we use the origin time estimate from the seismic arrival time (Table 2, Garcia et al., 2022). The infrasound source is at the crater associated to the events. The satellite images of these craters provide the exact distances and backazimuth (Table 2). Note that these distances and backazimuth are matched closely by analysis of the two seismic recordings, e.g. body-wave arrival times and chirp polarization (Garcia et al., 2022). We focus on the vertical and radial components, where the radial direction is parallel to a great path from the seismic source to InSight. For the seismic recordings of the two events, we rotate the north and east components to the radial direction based on the backazimuth (Table 2). We apply a bandpass filter to the components of each chirp. For each chirp, we choose the filter band to have high signal-to-noise ratios and to avoid spectral anomaly like the sharp amplitude drop at 2.3 Hz in the S0986c vertical component (Figure 4). In the following waveform fitting, we refer to the filtered data as real data. A chirp also exists in the S0793a recording. However, that chirp displays complex properties (e.g. higher-mode), which deserve to be discussed independently (Section 5.2).

We compute the misfit between the synthetic and real chirps like

$$\chi = \sum_j \frac{1}{T} \int_T \left| \frac{u_z(s_j)}{\max(|u_z(s_j)|)} - \frac{u_z^o(s_j)}{\max(|u_z^o(s_j)|)} \right| + \left| \frac{u_x(s_j)}{\max(|u_z(s_j)|)} - \frac{u_x^o(s_j)}{\max(|u_z^o(s_j)|)} \right| dt \quad (22)$$

where s_j represents each event; the integral is done in the time window of each chirp (Figure 4) and T is the time window length for each chirp. We fix the first and third layers of the model, and only vary the V_S and the layer thickness of the second layer to find the misfit minimum (Figure 5). The S0981c misfit mainly varies with the layer thickness but does not change obviously with V_S when the thickness is less than 40 m (Figure 5a). The S0986c misfit presents a sloping area (Figure 5b) where the different combinations of the two parameters give similar misfits, which is known as trade-off in the geophysical inverse theory. In the total misfit of the two events (Figure 5c), the V_S and the layer thickness from the minimum provide good waveform fitting between the synthetic and real chirps (Figure 4). We discuss this model in the geological context in Section 5.1.

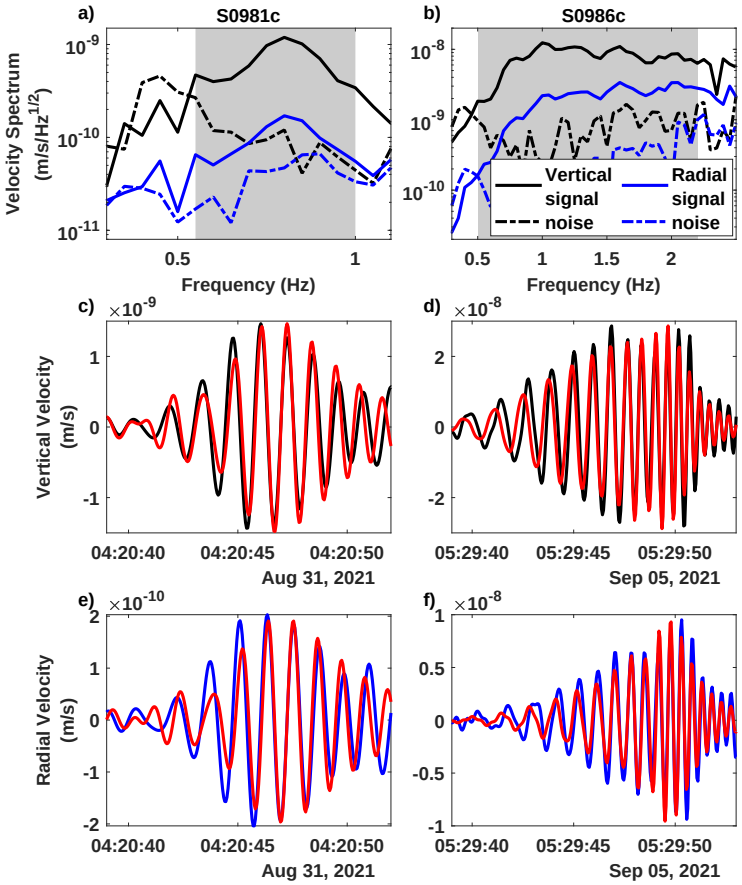

Figure 4. The vertical- and radial-component amplitude spectra of the chirps and noise (a,b) and the waveform fitting of the chirps in the time domain (c,d,e,f). The black and blue waveforms are the observed data and the red waveforms are the synthetic data. For each event, the signal spectra are from the time window used in the second and third rows, and the noise spectra are from the same-window-length recordings before the chirp. The gray areas indicate the frequency bands used in filtering the chirps, from 0.55 to 0.9 Hz for S0981c and from 0.5 to 2.2 Hz for S0986c.

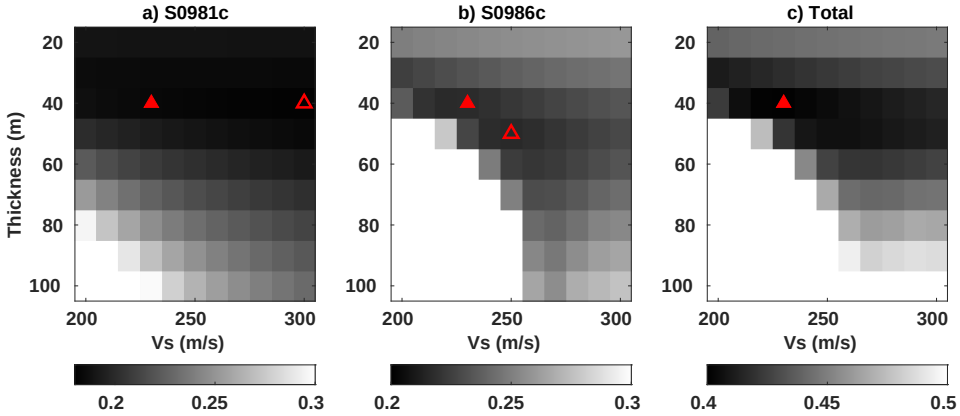

Figure 5. The misfit between the synthetic and observed chirp signals varies with the V_S and the thickness of the second subsurface layer (Table 1). The gray color indicates the misfit value. The red triangles correspond to the least misfit of the two events, while the empty triangle (a,b) corresponds to the least misfit of each event. The empty areas are the parameter combinations where the misfit values are larger than the color bar maximum or an air-coupled Rayleigh wave is excited.

5 Discussion

Our analytical waveform modelling aid us validating the Martian subsurface models from other observations (Section 5.1). By combining our modelling and the Martian atmospheric model, we provide an explanation for the S0793a seismic observation (Section 5.2). We also discuss how to improve our modelling in the future (Section 5.3 and 5.4).

5.1 Implication for the subsurface structure

Our waveform fitting provides a velocity model where the V_S increases with depth (Table 1). In this model, the first layer is interpreted as fine-sand-dominated regolith (e.g. Grott et al., 2021). Compared to the V_S of the first layer, the second-layer V_S is larger and thus corresponds well to a coarse regolith where pebbles exist. The second layer is of 40-m thickness, close to the estimate of the maximum surficial regolith thickness around InSight; however, the geological model beneath the InSight indicates that this coarse regolith layer is interrupted by a basalt layer (e.g. Warner et al., 2022). Note that the geological model is built by considering the velocity models from the horizontal-to-vertical (H/V) ratio measurement of the InSight ambient seismic vibration (Hobiger et al., 2021); we refer to the velocity models as the H/V models. To further investigate this layer thickness contradiction, we check how the synthetic waveforms from the H/V models fit the chirps.

We choose one of the H/V models (Figure 6a), which is close to the geological model, and then generate the synthetic waveforms (Figure 6b-e) following our computation in Section 4. We notice that for S0981c, the radial-component waveform of the H/V model possesses larger amplitudes than the observed chirp; for S0986c, the radial component from the H/V model does not fit the observed waveform around 5:29:50. The total misfit of the H/V model (Equation 22) is 0.44, 15% larger than the total misfit of our three-layer model, 0.40. Thus our model provides a better waveform fitting to the chirps than the H/V model. We repeat the above process with the other three H/V models (Figure S2,S3,S4). We notice that all the three models provides smaller radial-component amplitudes compared to the real chirps.

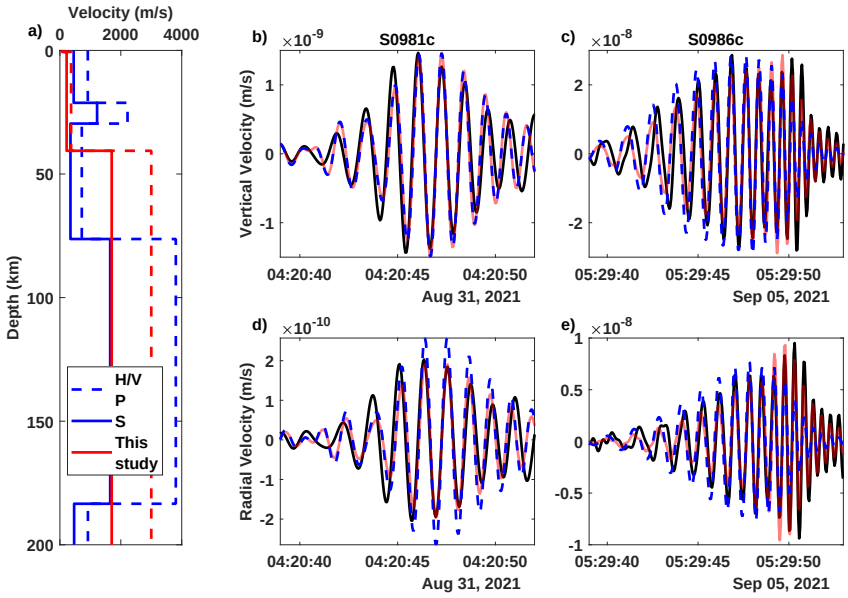

Figure 6. Comparison of the chirp waveform fitting between the H/V and the 3-layer models. The H/V model (blue) is the weakly-constrained maximum a posteriori estimation from Hobiger et al. (2021) and provides the blue dashed waveforms (b,c,d,e). The black and red waveforms (b,c,d,e) are the same observed and synthetic chirps from Figure 4, respectively.

The synthetic waveforms from the H/V models fit the vertical component of the recordings (Figure 6,S2,S3,S4). Thus the H/V models does not contradict with the chirp observation. Meanwhile, this waveform fitting difference between the H/V and our models could be due to the different sensitivities of the H/V ratio and the compliance to a same elastic property (e.g. Maupin, 2017; Kenda et al., 2020). Therefore, even through our model explain the chirps better than the H/V models, we cannot determine if our model is closer to the real subsurface than the H/V models. In order to achieve an accurate subsurface model, we need to incorporate the chirp observation, the H/V ratio measures, and other available data like the normalized compliance measures from the Martian pressure drops (e.g. Kenda et al., 2020; Onodera, 2022).

5.2 Higher-mode guided infrasound from the atmospheric model

The S0793a seismic recording includes a chirp signal in the time domain (Figure 7a). However, in opposition to the S0986c and S0981c group velocity measurement, which yields a single monotonous trend (Figure 3c and S1b), the measurement of the S0793a chirp provides two trends (Figure 7b): a horizontal one from 1 to 2 Hz at around 251 m/s, and a sloping one with decreasing velocity, from about 1.2 Hz to 2.3 Hz. The horizontal trend may correspond to an infrasound propagating directly from the impact and requires further investigation. It is ambiguous to attribute the sloping trend to a guided infrasound, since the bandwidth of the trend is short and the trend is not as continuous as the ones of S0981c and S0986c (Figure S1b and S1c). In the rest of this subsection, we present that the sloping trend can be explained by the higher-mode guided infrasound, while we also recognize that there could be other interpretations for the trend like the scattered infrasound (i.e. echoes, Garcia et al., 2022).

We compute the fundamental- and 1st-higher-mode group velocities and the eigenfunctions of this guided infrasound by applying our computation (Section 2) to the corresponding infrasound velocity model (Figure 7c). The synthetic fundamental-mode group

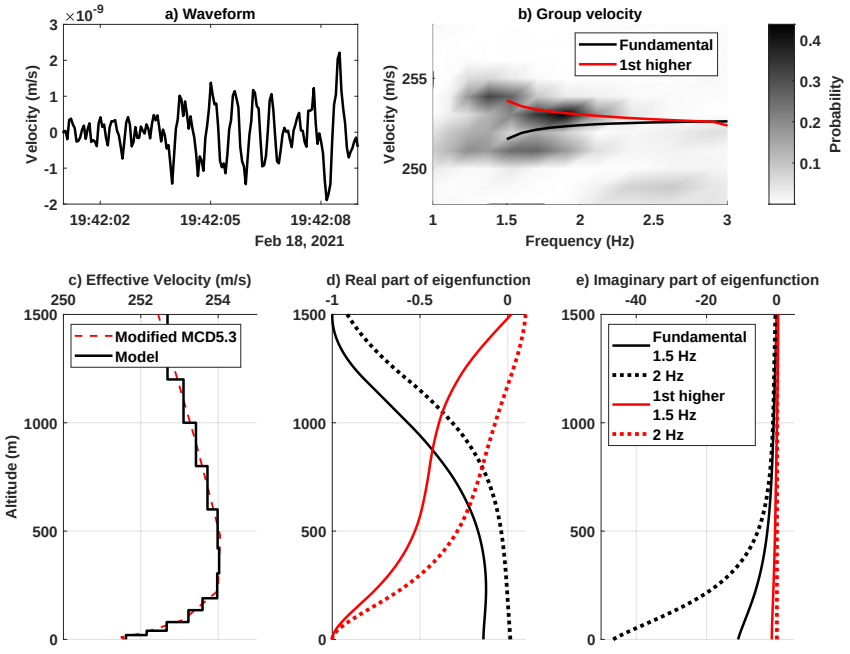

Figure 7. (a) The S0793a chirp bandpass filtered between 0.5 and 8 Hz. (b) Comparison of the group-velocity measurement from the chirp (gray) to the synthetic group velocity of the fundamental- and 1st-higher mode. These modes are from a 1D layered model modified from the MCD model (c, Table S1). We also compute the eigenfunctions corresponding to these modes and normalize each eigenfunction by its maximum real value (d and e).

velocity increases with increasing frequency, opposite of the measured group velocity (black curve in Figure 7b). The fundamental-mode eigenfunctions are complex valued, instead of real valued as in S0986c (Section 3b). The real parts of the eigenfunctions are close to zero on the ground surface and increase from the surface to the 1500-m altitude (Figure 7d). This means that this fundamental-mode guided infrasound possesses smaller amplitude on the ground surface than at 1500 m altitude. The imaginary parts of the eigenfunctions are large near the ground surface (Figure 7e) and represent energy leakage of the guided infrasound to the top halfspace (e.g. Press & Harkrider, 1962; Radovich & De Bremaecker, 1974). Thus this fundamental mode possesses weak pressure on the ground surface.

The 1st-higher-mode guided infrasound of the S0793a atmosphere model possesses a stronger pressure than the fundamental-mode on the ground surface (Figure S1d). We notice that the 1st-higher-mode group velocity agrees with the ground-velocity measurement (the sloping trend in Figure 7b). Furthermore, the real part of the 1st-higher-mode eigenfunctions presents a maximum absolute value on the ground surface, while the imaginary part is close to zero on the ground surface compared to the fundamental-mode. Therefore, the 1st-higher-mode guided infrasound could generate the recorded S0793a chirp.

5.3 The free surface boundary condition

On the ground surface, the vertical particle velocity (v_z) in the atmosphere is equal to the vertical ground velocity (u_z). This yields:

$$v_z(z=0) = -u_z(z=0), \tag{23}$$

where the minus sign is due to different conversion of the positive z-axis direction in atmosphere (altitude) and the subsurface (depth). The formula above and Equation 4 lead to

$$\partial_z p(z=0) = \rho(\partial_t + w_x \partial_x) u_z(z=0), \tag{24}$$

where ρ is the air density. We rewrite this equation as

$$\partial_z P(z=0) = -i\rho(\omega - w_x k)\frac{U_z(z=0)}{T_{zz}(z=0)} P(z=0), \tag{25a}$$

$$= -i\rho(\omega - w_x k) C_z P(z=0). \tag{25b}$$

The expected value for C_z on Mars is around $10^{-5} m/s/Pa$ and ρ is about $0.02 kg/m^3$. Thus, between 0.5 and 3 Hz, $\partial_z P(z=0)$ is on the order of 10^{-5} of $P(z=0)$. We can conclude that the guided-infrasound atmospheric pressure is almost constant near the ground surface and thus $v_z \approx 0$ (Equation 4). This justifies the rigid ground-surface boundary condition used in our derivation of guided infrasound (Equation 7). Our benchmark (Appendix B) also validates that our modelling result agrees well with the numerical simulation where v_z is continuous on the ground surface, the atmosphere-solid-earth boundary.

We notice that the continuous-v_z boundary condition is necessary for modelling the coupled normal mode between a planet atmosphere and the solid planet (e.g. Watada, 1995; Lognonné et al., 1998; Tanimoto, 2001). Thus in order to be able to model the coupled mode, we will incorporate this boundary condition into our modelling in future.

5.4 Potential improvement and future work

In our forward modelling, we assume the boundary between the atmosphere and the ground to be flat. However, the ground surface topography affects the compliance (e.g. Bishop et al., 2021) by altering the guided infrasound horizontal wavenumber relative to the ground surface. To incorporate the topography into the compliance computation, we can compute the spatial wavenumber of the topography and combine the wavenumber with the one of guided infrasound, similar to the microseism studies which consider ocean waves coupling with topographic seafloors (e.g. Ardhuin et al., 2015).

Since our forward modelling is fast in computation, one can adopt this modelling to perform a Markov-chain Monte Carlo inversion of the atmospheric and subsurface parameters from the chirp signals. A Markov-chain Monte Carlo inversion explores different parameter combinations (e.g. Tarantola, 2005). As we demonstrate the trade-off between the shear-wave velocity and layer thickness in our three-layer subsurface model (Section 4), we expect more parameter trade-offs if the subsurface model possesses more than three layers. We also expect a trade-off between the atmospheric and subsurface parameters, since the compliance computation depends on the guided-infrasound phase velocity from the atmospheric model. Thus the inversion could aid us to assess these trade-offs between both the atmospheric (like infrasound velocity) and the subsurface (e.g. Vs and layer thickness) parameters.

6 Conclusion

We analytically model chirp, the seismic waveform due to the coupling between guided infrasound and the ground. We theoretically demonstrate the guided-infrasound propagation in a 1D atmospheric model and compute the guided-infrasound phase and group velocities. Our group velocities match well with the measures from the S0981c and S098c chirp observation on Mars. We convert the guided infrasound into a chirp through compliance of a three-layer subsurface velocity model. We validate our modelling through a benchmark.

By applying our modelling to the Martian atmospheric model, we model synthetic chirps to fit the real chirp recordings of S0981c and S0986c. Through the waveform fitting, we achieve a three-layer Martian subsurface velocity model, where the coarse regolith is 40-m thick. We also apply our modelling to examine the velocity models from the InSight ambient-seismic-vibration H/V ratio observation and present that these models explain a part of the chirp recordings but do not provide a good fitting as our three-layer model. Therefore we need to incorporate all the available observations to constrain the Martian subsurface structure estimation.

7 Open Research and Data Availability Statement

The Martian topography data are from the NASA PDS Geosciences Node (Neumann et al., 2003) The InSight seismic waveform data are available from the IPGP Datacenter, IRIS-DMC and the NASA PDS (InSight Mars SEIS Data Service, 2019a, 2019b). The Martian atmospheric parameters are from MCD (Millour et al., 2018). The codes for computation of the guided infrasound are available in Xu (2022).

Appendix A Guided infrasound on Earth

We present a terrestrial example of chirp, where the infrasound source is the 2017-12-12 Baumgarten gas hub explosion in Austria. This event generates both seismic waves and infrasound. These infrasound couples to the ground and are recorded by local seismic stations (Schneider et al., 2018). From these stations, we choose one from AlpArray (Hetényi et al., 2018), A333A (Figure A1), at the northeast of the explosion. The A333A vertical-component recording presents a chirp (Figure A1b), from which we measure the group velocity (Figure A1d). Our group-velocity measurement method is detailed in Panning et al. (2015) and Drilleau et al. (2020). We choose an atmospheric profile used in Schneider et al. (2018) and follow the computation in Section 2 to compute the synthetic group velocity. The difference between the measured and synthetic group velocity indicates that we can improve the Earth low-altitude (<3000 m) atmospheric model using the guided infrasound.

Appendix B Benchmark

We benchmark our modelling against a numerical simulation software, SPECFEM2D-DG (Martire et al., 2020). SPECFEM2D-DG can model acoustic and seismic waves in a coupled solid-fluid system. Garcia et al. (2022) utilize this software to simulate the seismic recording at InSight location due to the S0793a, S0981c, and S0986c impacts. We choose the S0981c simulation result in this benchmark. Garcia et al. (2022) use the S0981c atmospheric model from MCD (Millour et al., 2018) and a four-layer subsurface model (Table B1). Garcia et al. (2022) set the pressure and seismic receivers 246 km away from the source and the seismic receiver at 5 m under the ground surface. We use the same models and the same receiver setting. We compare our modelling result to the one from Garcia et al. (2022): the group velocity (Figure B1a), the compliance (Figure B1b), and the pressure and seismic waveforms (Figure B2). Those match well in the frequency domain or the time domain. Note that in the seismic waveform comparison, since SPECFEM2D-DG is for the 2D space, instead of the 3D, we have to modify Equation 20 and 20 by removing the 3D cylindrical wave term:

$$u_z = \mathscr{F}^{-1}\left[S(\omega)\exp\left(-ikx - ax\right)\frac{P^2(\omega,0)}{\int P^2(\omega,z)dz}C_z(\omega)\right], \tag{B1}$$

$$u_x = \mathscr{F}^{-1}\left[S(\omega)\exp\left(-ikx - ax\right)\frac{P^2(\omega,0)}{\int P^2(\omega,z)dz}C_x(\omega)\right]. \tag{B2}$$

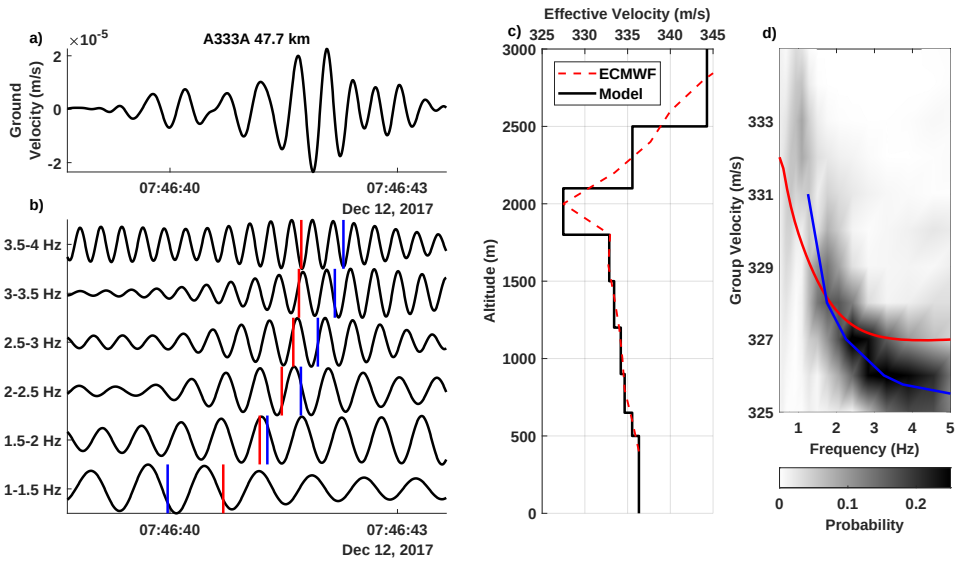

Figure A1. Illustration of the A333A chirp (a,b) and computation of the group velocity (c,d). We bandpass filter the A333A vertical-component velocity recording between 0.5 and 5 Hz (a) and in multiple narrow bands (b). We measure group velocity from the recording (a) and pick the probability maximum at each frequency as the group velocity (blue line in d). Based on the ECMWF profile used in Schneider et al. (2018), we plot the effective acoustic-wave velocity profile (red dashed line in c) and the 1D layered model (black line in c). From the 1D model, we compute the synthetic group velocity (red line in d). We convert the synthetic and measured group velocities at the narrow bands to the corresponding arrival times (red and blue bars in b).

Table B1. The subsurface velocity model used in (Garcia et al., 2022). Note that we only use this model in the benchmark section.

Layer number	$V_P(m/s)$	$V_S(m/s)$	Density (kg/m^3)	Thickness (m)
1	744	398	1800	100
2	3800	1850	2304	9900
3	4500	2800	2570	14000
4	6224	3753	2863	∞

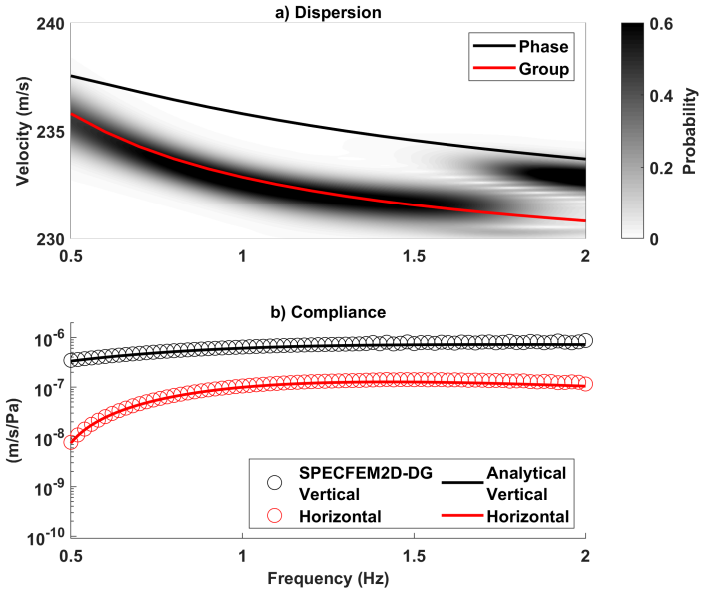

Figure B1. The comparison of the group velocity and compliance from our analytical approach to SPECFEM2D-DG. The group velocity measurement and compliance values from SPECFEM2D-DG are the gray background (a) and the empty circles (b), respectively. The estimates from our analytical approach are in the curves (a,b).

Acknowledgments

The authors acknowledge the NASA, the CNES, their partner agencies and Institutions (UKSA, SSO, DLR, JPL, IPGP-CNRS, ETHZ, IC, and MPS-MPG) and the flight operations team at JPL, SISMOC, MSDS, IRIS-DMC, and PDS for providing the SEED SEIS data. This study is InSight contribution number 242 and LA-UR-22-25146. ZX thanks Eléonore Stutzmann, Ludovic Margerin, Dylan Mikesell for fruitful discussion. ZX also thanks Aymeric Spiga's help in accessing the Earth atmospheric model and discussion about the Mars atmosphere. The authors thank the AlpArray Seismic Network Team; the authors thank Wayne Crawford, Stefan Heimers, and John Clinton for their help in accessing the AlpArray data. The authors also thank Felix M. Schneider for providing the conversion from the atmospheric temperature to acoustic-wave velocity. The authors thank editor Laurent Montési, reviewer Toshiro Tanimoto, and an anonymous reviewer for their constructive feedback that helped improve this manuscript. This research is supported by ANR MAGIS (ANR-19-CE31-0008-08) and the Initiative d'Excellence (IdEx) Université Paris Cité (ANR-18-IDEX-0001). MF is funded by the Center for Space and Earth Science of LANL.

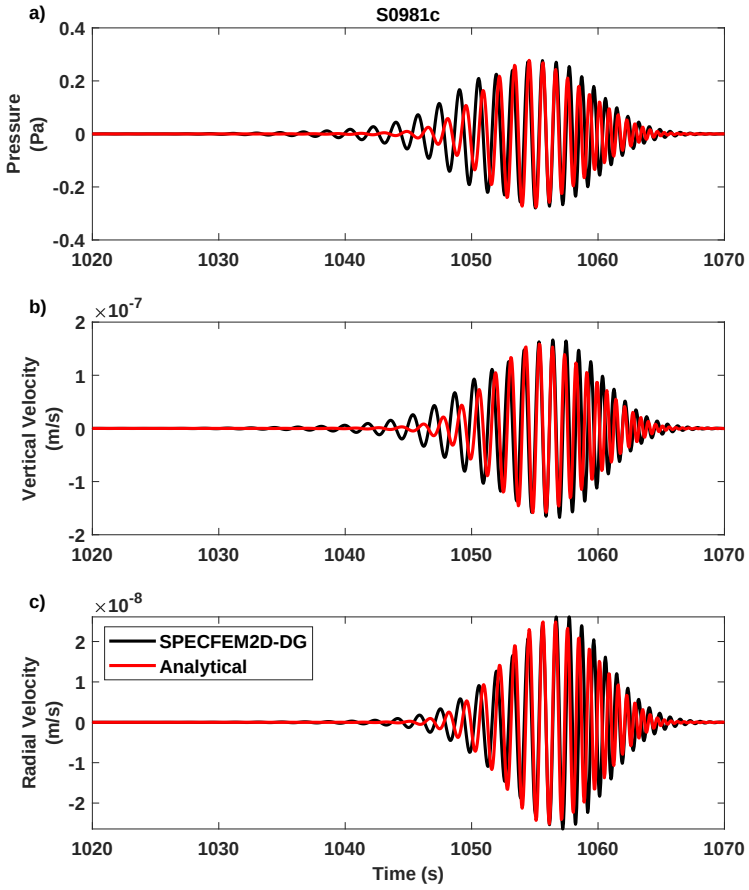

Figure B2. The waveform comparison of the atmospheric pressure, vertical velocity, and horizontal velocity from our analytical approach to SPECFEM2D-DG. The waveforms are all bandpass filtered between 0.5 and 2 Hz. We normalize our waveforms by the maximum value of the pressure from SPECFEM2D-DG.

References

Aki, K., & Richards, P. G. (2002). *Quantitative seismology.*

Ardhuin, F., Gualtieri, L., & Stutzmann, E. (2015). How ocean waves rock the Earth: Two mechanisms explain microseisms with periods 3 to 300 s. *Geophysical Research Letters*, *42*(3), 765–772.

Assink, J. D. (2012). Infrasound as upper atmospheric monitor. *Ph. D. Thesis*.

Banerdt, W. B., Smrekar, S. E., Banfield, D., Giardini, D., Golombek, M., Johnson, C. L., ... others (2020). Initial results from the InSight mission on Mars. *Nature Geoscience*, *13*(3), 183–189.

Banfield, D., Rodriguez-Manfredi, J., Russell, C., Rowe, K., Leneman, D., Lai, H., ... others (2019). InSight auxiliary payload sensor suite (APSS). *Space Science Reviews*, *215*(1), 1–33.

Bass, H. E., & Chambers, J. P. (2001). Absorption of sound in the Martian atmosphere. *The Journal of the Acoustical Society of America*, *109*(6), 3069–3071.

Ben-Menahem, A., & Singh, S. J. (2012). *Seismic waves and sources.* Springer Science & Business Media.

Bishop, J. W., Fee, D., Modrak, R., Tape, C., & Kim, K. (2021). Spectral element modeling of acoustic to seismic coupling over topography. *Journal of Geophysical Research: Solid Earth*, e2021JB023142.

Chakravarthy, G. V. R. (2008). Love Wave Propagation in Viscoelastic Media. *Boise State University Theses and Dissertations*.

Clinton, J. F., Ceylan, S., van Driel, M., Giardini, D., Stähler, S. C., Böse, M., ... others (2021). The Marsquake catalogue from InSight, sols 0–478. *Physics of the Earth and Planetary Interiors*, *310*, 106595.

Drilleau, M., Beucler, E., Lognonné, P., Panning, M. P., Knapmeyer-Endrun, B., Banerdt, W. B., ... others (2020). MSS/1: Single-station and single-event marsquake inversion. *Earth and Space Science*, *7*(12), e2020EA001118.

Edwards, W. N., Eaton, D. W., & Brown, P. G. (2008). Seismic observations of meteors: Coupling theory and observations. *Reviews of Geophysics*, *46*(4).

Ewing, W. M., Jardetzky, W. S., Press, F., & Beiser, A. (1957). *Elastic waves in layered media.*

Garcia, R. F., Brissaud, Q., Rolland, L., Martin, R., Komatitsch, D., Spiga, A., ... Banerdt, B. (2017). Finite-difference modeling of acoustic and gravity wave propagation in Mars atmosphere: application to infrasounds emitted by meteor impacts. *Space Science Reviews*, *211*(1), 547–570.

Garcia, R. F., Daubar, I. J., Beucler, É., Posiolova, L., Collins, G. S., Lognonné, P., ... others (2022). Seismological location and orbital imaging of newly formed craters on Mars. *Nature Geosciences*, online. doi: 10.1038/s41561-022-01014-0

Garcia, R. F., Kenda, B., Kawamura, T., Spiga, A., Murdoch, N., Lognonné, P. H., ... others (2020). Pressure effects on the SEIS-InSight instrument, improvement of seismic records, and characterization of long period atmospheric waves from ground displacements. *Journal of Geophysical Research: Planets*, *125*(7), e2019JE006278.

Gardner, G., Gardner, L., & Gregory, A. (1974). Formation velocity and density—The diagnostic basics for stratigraphic traps. *Geophysics*, *39*(6), 770–780.

Giardini, D., Lognonné, P., Banerdt, W. B., Pike, W. T., Christensen, U., Ceylan, S., ... others (2020). The seismicity of Mars. *Nature Geoscience*, *13*(3), 205–212.

Gibbons, S. J., Ringdal, F., & Kværna, T. (2007). Joint seismic-infrasonic processing of recordings from a repeating source of atmospheric explosions. *The Journal of the Acoustical Society of America*, *122*(5), EL158–EL164.

Grott, M., Spohn, T., Knollenberg, J., Krause, C., Hudson, T. L., Piqueux, S., ... others (2021). Thermal conductivity of the Martian soil at the InSight landing

site from HP3 active heating experiments. *Journal of Geophysical Research: Planets*, *126*(7), e2021JE006861.

Harkrider, D. G. (1964). Theoretical and observed acoustic-gravity waves from explosive sources in the atmosphere. *Journal of Geophysical Research*, *69*(24), 5295–5321.

Herrin, E. T., Kim, T. S., & Stump, B. W. (2006). Evidence for an infrasound waveguide. *Geophysical research letters*, *33*(7).

Hetényi, G., Molinari, I., Clinton, J., Bokelmann, G., Bondár, I., Crawford, W. C., ... others (2018). The AlpArray seismic network: a large-scale European experiment to image the Alpine orogen. *Surveys in geophysics*, *39*(5), 1009–1033.

Hobiger, M., Hallo, M., Schmelzbach, C., Stähler, S., Fäh, D., Giardini, D., ... others (2021). The shallow structure of Mars at the InSight landing site from inversion of ambient vibrations. *Nature communications*, *12*(1), 1–13.

Ichihara, M., Takeo, M., Yokoo, A., Oikawa, J., & Ohminato, T. (2012). Monitoring volcanic activity using correlation patterns between infrasound and ground motion. *Geophysical Research Letters*, *39*(4).

InSight Mars SEIS Data Service. (2019a). *Data Service, InSight SEIS Data Bundle.* PDS Geosciences (GEO) Node. doi: 10.17189/1517570

InSight Mars SEIS Data Service. (2019b). *SEIS raw data, InSight mission.* IPGP, JPL, CNES, ETHZ, ICL, MPS, ISAE-Supaero, LPG, MFSC. doi: https://doi.org/10.18715/SEIS.INSIGHT.XB

Kenda, B., Drilleau, M., Garcia, R. F., Kawamura, T., Murdoch, N., Compaire, N., ... others (2020). Subsurface structure at the InSight landing site from compliance measurements by seismic and meteorological experiments. *Journal of Geophysical Research: Planets*, *125*(6), e2020JE006387.

Kenda, B., Lognonné, P., Spiga, A., Kawamura, T., Kedar, S., Banerdt, W. B., ... Golombek, M. (2017). Modeling of ground deformation and shallow surface waves generated by Martian dust devils and perspectives for near-surface structure inversion. *Space Science Reviews*, *211*(1), 501–524.

Landau, L. D., & Lifshitz, E. M. (2013). *Fluid mechanics: Landau and lifshitz: Course of theoretical physics, volume 6* (Vol. 6). Elsevier.

Langston, C. A. (2004). Seismic ground motions from a bolide shock wave. *Journal of Geophysical Research: Solid Earth*, *109*(B12).

Lognonné, P., Banerdt, W., Pike, W., Giardini, D., Christensen, U., Garcia, R. F., ... others (2020). Constraints on the shallow elastic and anelastic structure of Mars from InSight seismic data. *Nature Geoscience*, *13*(3), 213–220.

Lognonné, P., Banerdt, W. B., Giardini, D., Pike, W. T., Christensen, U., Laudet, P., ... others (2019). SEIS: Insight's seismic experiment for internal structure of Mars. *Space Science Reviews*, *215*(1), 1–170.

Lognonné, P., Clévédé, E., & Kanamori, H. (1998). Computation of seismograms and atmospheric oscillations by normal-mode summation for a spherical earth model with realistic atmosphere. *Geophysical Journal International*, *135*(2), 388–406.

Lorenz, R. D., Kedar, S., Murdoch, N., Lognonné, P., Kawamura, T., Mimoun, D., & Bruce Banerdt, W. (2015). Seismometer detection of dust devil vortices by ground tilt. *Bulletin of the Seismological Society of America*, *105*(6), 3015–3023.

Martire, L., Garcia, R. F., Rolland, L., Spiga, A., Lognonné, P. H., Banfield, D., ... Martin, R. (2020). Martian infrasound: Numerical modeling and analysis of InSight's data. *Journal of Geophysical Research: Planets*, *125*(6), e2020JE006376.

Maupin, V. (2017). 3-D sensitivity kernels of the Rayleigh wave ellipticity. *Geophysical Journal International*, *211*(1), 107–119.

Millour, E., Forget, F., Spiga, A., Vals, M., Zakharov, V., & Montabone, L. (2018).

Mars Climate Database. *From Mars Express to ExoMars*, 68.

Morgan, P., Grott, M., Knapmeyer-Endrun, B., Golombek, M., Delage, P., Lognonné, P., ... others (2018). A pre-landing assessment of regolith properties at the InSight landing site. *Space Science Reviews*, *214*(6), 1–47.

Negraru, P. T., & Herrin, E. T. (2009). On infrasound waveguides and dispersion. *Seismological Research Letters*, *80*(4), 565–571.

Neumann, G. A., Abshire, J. B., Aharonson, O., Garvin, J. B., Sun, X., & Zuber, M. T. (2003). Mars Orbiter Laser Altimeter pulse width measurements and footprint-scale roughness. *Geophysical research letters*, *30*(11).

Nijs, L., & Wapenaar, C. (1990). The influence of wind and temperature gradients on sound propagation, calculated with the two-way wave equation. *The Journal of the Acoustical Society of America*, *87*(5), 1987–1998.

Nijs, L., & Wapenaar, C. (1992). Reply to:"Comments on the influence of wind and temperature gradients on sound propagation calculated with the two-way wave equation"[J. Acoust. Soc. Am. 9 1, 498–500 (1992)]. *The Journal of the Acoustical Society of America*, *91*(1), 501–504.

Onodera, K. (2022). Subsurface structure of the Moon and Mars deduced from 3D seismic wave propagation simulation and analysis of Apollo and InSight seismic data. *Doctoral dissertation of The Graduate University for Advanced Studies, SOKENDAI and Université de Paris Cité*.

Panning, M. P., Beucler, É., Drilleau, M., Mocquet, A., Lognonné, P., & Banerdt, W. B. (2015). Verifying single-station seismic approaches using Earth-based data: Preparation for data return from the InSight mission to Mars. *Icarus*, *248*, 230–242.

Pekeris, C. (1948). The propagation of a pulse in the atmosphere. Part II. *Physical Review*, *73*(2), 145.

Pierce, A. D. (1990). Wave equation for sound in fluids with unsteady inhomogeneous flow. *The Journal of the Acoustical Society of America*, *87*(6), 2292–2299.

Press, F., & Harkrider, D. (1962). Propagation of acoustic-gravity waves in the atmosphere. *Journal of Geophysical Research*, *67*(10), 3889–3908.

Radovich, B., & De Bremaecker, J. C. (1974). Body waves as normal and leaking modes—leaking modes of Love waves. *Bulletin of the Seismological Society of America*, *64*(2), 301–306.

Schneider, F. M., Fuchs, F., Kolínskỳ, P., Caffagni, E., Serafin, S., Dorninger, M., ... others (2018). Seismo-acoustic signals of the Baumgarten (Austria) gas explosion detected by the AlpArray seismic network. *Earth and Planetary Science Letters*, *502*, 104–114.

Smith, D. E., Zuber, M. T., Frey, H. V., Garvin, J. B., Head, J. W., Muhleman, D. O., ... others (2001). Mars Orbiter Laser Altimeter: Experiment summary after the first year of global mapping of Mars. *Journal of Geophysical Research: Planets*, *106*(E10), 23689–23722.

Sorrells, G. G. (1971). A preliminary investigation into the relationship between long-period seismic noise and local fluctuations in the atmospheric pressure field. *Geophysical Journal International*, *26*(1-4), 71–82.

Sorrells, G. G., McDonald, J. A., Der, Z., & Herrin, E. (1971). Earth motion caused by local atmospheric pressure changes. *Geophysical Journal International*, *26*(1-4), 83–98.

Stutzmann, É., Schimmel, M., Lognonné, P., Horleston, A., Ceylan, S., van Driel, M., ... others (2021). The polarization of ambient noise on Mars. *Journal of Geophysical Research: Planets*, *126*(1), e2020JE006545.

Tanimoto, T. (2001). Continuous free oscillations: atmosphere-solid earth coupling. *Annual Review of Earth and Planetary Sciences*, *29*(1), 563–584.

Tanimoto, T., & Wang, J. (2019). Theory for deriving shallow elasticity structure from colocated seismic and pressure data. *Journal of Geophysical Research:*

Solid Earth, *124*(6), 5811–5835.

Tarantola, A. (2005). *Inverse problem theory and methods for model parameter estimation* (Vol. 89). siam.

Warner, N., Golombek, M., Ansan, V., Marteau, E., Williams, N., Grant, J., ... others (2022). In Situ and Orbital Stratigraphic Characterization of the InSight Landing Site–A Type Example of a Regolith-Covered Lava Plain on Mars. *Journal of Geophysical Research: Planets*, e2022JE007232.

Warner, N., Golombek, M., Sweeney, J., Fergason, R., Kirk, R., & Schwartz, C. (2017). Near surface stratigraphy and regolith production in southwestern elysium planitia, mars: implications for hesperian-amazonian terrains and the insight lander mission. *Space Science Reviews*, *211*(1), 147–190.

Watada, S. (1995). Part I. Near-source acoustic coupling between the atmosphere and the solid earth during volcanic eruptions. Part II. Nearfield normal mode amplitude anomalies of the Landers earthquake. *Doctoral dissertation of California Institute of Technology*. doi: 10.7907/JSE5-G397

Waxler, R. (2002). A vertical eigenfunction expansion for the propagation of sound in a downward-refracting atmosphere over a complex impedance plane. *The Journal of the Acoustical Society of America*, *112*(6), 2540–2552.

Waxler, R. (2004). Modal expansions for sound propagation in the nocturnal boundary layer. *The Journal of the Acoustical Society of America*, *115*(4), 1437–1448.

Xu, Z. (2022). *ZongboXu/HFGI: v1.0.0 (Version v1.0.0).* [Software] Zenodo. doi: https://doi.org/10.5281/zenodo.7079346